ADVANCED FUNCTIONAL MATERIALS
www.afm-journal.de

Ultrastable Perovskite Encased in a Helical Cage for Tunable Full-Color Mirror-Image Circularly Polarized Luminescence

Deblina Das, Youngsin Park, Sourav Mal, Kwangseuk Kyhm, Robert A. Taylor, Atanu Jana, and Sangeun Cho**

Achieving stable and efficient circularly polarized luminescence (CPL) from achiral perovskite nanocrystals (PNCs) remains a major challenge in the development of advanced chiroptical materials. Herein, the syntheses of a total of nine compounds, including full-color colloidal polymer-capped PNC composites are reported based on organic-inorganic hybrid perovskites and inorganic 2D nanosheets (NSs) using phenacyl halide as a single organic source of halide precursor. While the initial PNCs exhibit low photoluminescence quantum yield (PL QY) and poor stability, a previously unexplored surface absorption/ion exchange strategy employing 2D-$ZrH_2P_2O_8$ NSs significantly enhances both optical properties and long-term stability, e.g., the $FAPbBr_3$@$ZrH_2P_2O_8$ (FA = formamidinium) composite exhibits a significantly enhanced PL QY of 88.57%, compared to 30.9% for the pristine counterparts, owing to the protective effect of the robust 2D $ZrH_2P_2O_8$ network that enhances stability under ambient conditions. Crucially, embedding these stabilized PNCs into a chiral polymer matrix induces distinct mirror-image strong CPL signals both in solution and solid-state. This rare dual-phase CPL activity arises from the conformational adaptability of the chiral polymer, which imparts chirality to the achiral PNCs via both covalent and non-covalent interactions. These findings present a versatile strategy for producing robust, CPL-active stable perovskite materials across the visible spectrum for next-generation chiroptoelectronic devices.

1. Introduction

Recent research in the chirality of organic–inorganic lead halide perovskite nanocrystals (PNCs) has opened new avenues for the development of advanced applications.[1–3] In particular, the bandgap-tunable photoluminescence (PL) properties of perovskites have made them highly attractive for use in optical applications and integrating these properties into circularly polarized luminescence (CPL) offers a novel spectral window for the development of advanced photonic and optoelectronic technologies.[4] CPL is generally achieved by generating chiral structural arrangements in emissive materials, with initial studies focusing on chiral lanthanide and actinide complexes.[5] However, despite achieving high luminescence dissymmetry factors (g_{lum} up to 1), these complexes are hindered by a low photoluminescence quantum yield (PL QY), which limits their practical applicability.[6,7] Recently, PNCs have achieved remarkable success in optoelectronic devices due to their unique PL properties, including a wide tunability, high PL QY (≈100%), and narrow emission bandwidth (≈20 nm).[8,9] These attributes have led to growing interest in PNCs[10] as promising candidates for CPL-active materials.[11–13] The introduction of chirality in perovskites has shown significant potential for enhancing their performance in spintronic applications,[14] 3D displays,[15] optical encryption,[16] photovoltaic applications,[17] and data storage.[18] Methods to induce chirality include post-synthetic ligand treatment, embedding NCs in chiral matrices, and utilizing chiral templates. For example, Kim et al. employed chiral ligands to modify the surface of pure formamidinium

D. Das, S. Mal, A. Jana, S. Cho
Division of System Semiconductor
College of AI Convergence
Dongguk University
Seoul 04620, Republic of Korea
E-mail: atanujana@dongguk.edu; sangeun.c@dongguk.edu

The ORCID identification number(s) for the author(s) of this article can be found under https://doi.org/10.1002/adfm.202514790

DOI: 10.1002/adfm.202514790

Y. Park
Department of Chemistry
School of Natural Science
Ulsan National Institute of Science and Technology (UNIST)
Ulsan 44919, Republic of Korea

K. Kyhm
Department of Opto-mechatronics Engineering
Pusan National University
Busan 46241, Republic of Korea

R. A. Taylor
Clarendon Laboratory
Department of Physics
University of Oxford
Oxford OX1 3PU, UK

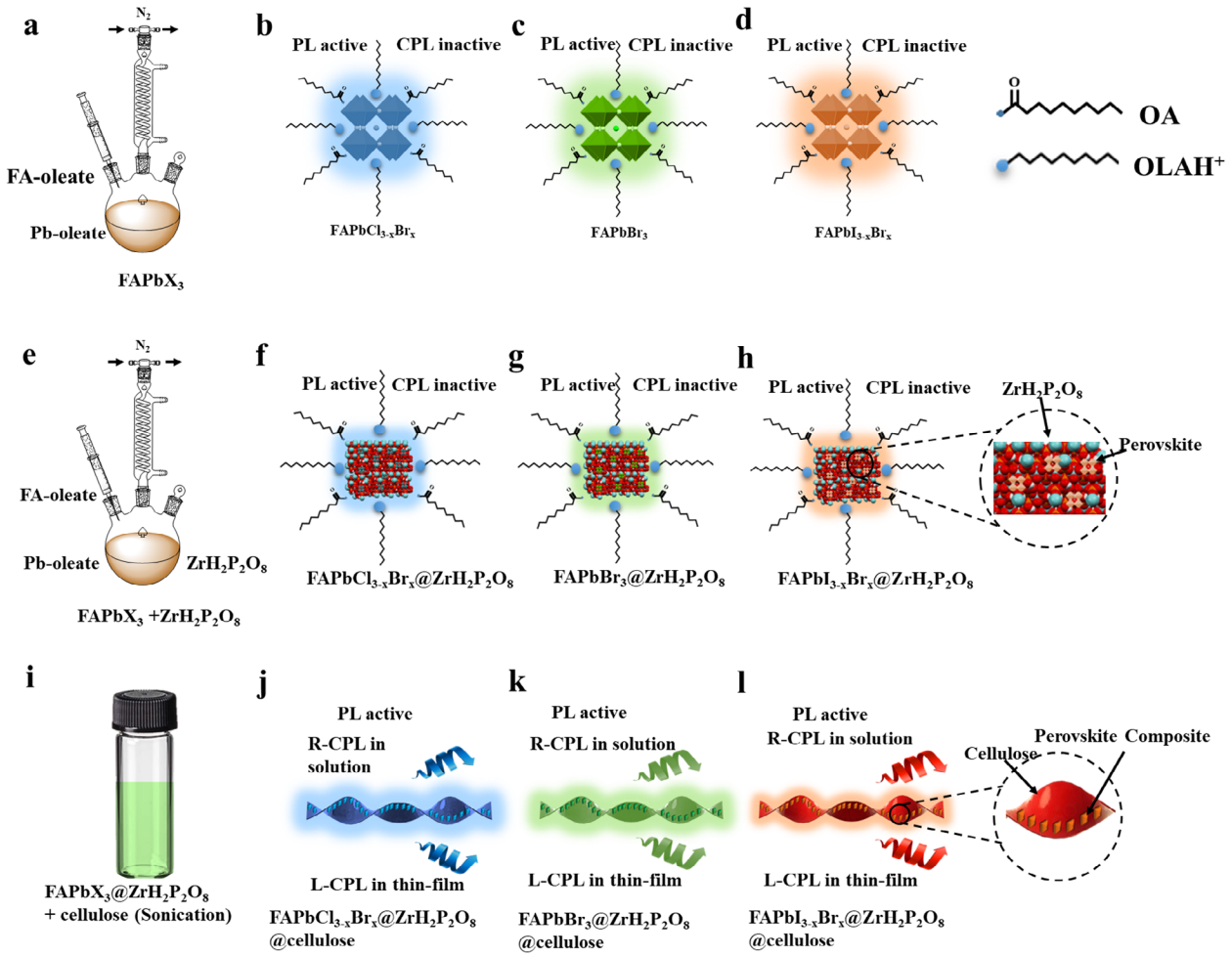

Scheme 1. Schematic illustrations of the fabrication of pure perovskite NCs, perovskite composite, and cellulose encapsulated perovskite composite, along with their PL and CPL properties. a) Synthesis scheme of $FAPbX_3$ NCs. b) $FAPbBr_{3-x}Cl_x$: PL active, CPL inactive. c) $FAPbBr_3$: PL active, CPL inactive. d) $FAPbBr_{3-x}I_x$: PL active, CPL inactive. e) Synthesis scheme of $FAPbX_3@ZrH_2P_2O_8$ composite materials. f) $FAPbBr_{3-x}Cl_x@ZrH_2P_2O_8$: PL active, CPL active. g) $FAPbBr_3@ZrH_2P_2O_8$: PL active, CPL inactive. h) $FAPbBr_{3-x}I_x$: PL active, CPL inactive. i) Synthesis process of $FAPbX_3@ZrH_2P_2O_8$@cellulose materials. j) $FAPbBr_{3-x}Cl_x@ZrH_2P_2O_8$@cellulose: PL active, CPL inactive. k) $FAPbBr_3@ZrH_2P_2O_8$@cellulose: PL active, CPL inactive. l) $FAPbBr_{3-x}I_x@ZrH_2P_2O_8$@cellulose: PL active, CPL inactive.

lead bromide ($FAPbBr_3$) PNCs, achieving moderate CPL activity.[19] Similarly, Tao et al. demonstrated that affixing chiral surface-passivating ligands could enhance film quality and CPL performance,[20] achieving a g_{lum} of 4×10^{-3}. Other approaches include embedding achiral PNCs into chiral matrices; this has been demonstrated by Gao et al., who utilized helical polymers to fabricate CPL-active hybrid nanofibers.[21] Zhao et al. advanced this further by employing chiral cellulose NC templates to influence perovskite symmetry and orientation in aqueous solutions, resulting in chiral NCs.[22] Current methods to stabilize perovskites often focus on green-emitting materials, with limited focus on the entire visible spectrum, while achieving colloidal stability, monodispersity, and defect suppression is challenging, hindering scalability and large-scale applications.

To address these limitations, researchers have explored innovative stabilization techniques without focusing on CPL properties. For example, Yang et al. demonstrated the use of polyvinylidene fluoride (PVDF) polymer matrices to stabilize $FAPbBr_3$ NCs, enhancing their PL QY and environmental resilience.[23] Zhu et al. also developed $FAPbBr_3$-poly(methyl methacrylate) (PMMA) composites with improved long-term stability,[10] while Perez et al. embedded $FAPbBr_3$ NCs into porous SiO_2 films, achieving a PL QY of 86% and enhanced durability.[24] In addition, a one-pot synthesis strategy introduced by Huo et al. employed A-SiO_2 and N—H bonding to produce stable $FAPbBr_3$ NCs.[25] However, these approaches often do not represent a universal solution for stabilizing PNCs across different emission wavelengths.

In this study, we aim to develop a broadband CPL-active perovskite system with enhanced structural stability and optical uniformity (**Scheme 1**). We adopt a rational materials design that combines a three-precursor synthesis of $FAPbX_3$ NCs with a novel growth strategy on layered 2D-$ZrH_2P_2O_8$ NSs, followed by chiral encapsulation using cellulose-based polymers. This multicomponent strategy enables precise control over composition, morphology, and interfacial properties, which are critical for achieving broadband and structurally stable CPL. By addressing long-standing challenges in spectral tunability, environmental

degradation, and defect-induced quenching, our approach lays the groundwork for scalable, chiroptically active materials compatible with next-generation optoelectronic devices.

2. Results

2.1. Synthesis Mechanisms for the $FAPbX_3@ZrH_2P_2O_8$ Composite

We stabilize $FAPbX_3$ PNCs through strong interfacial interactions with $ZrH_2P_2O_8$ NSs. FA^+ ions undergo ion exchange with surface protons on hydrogen phosphate groups, enriching the local FA^+ concentration and promoting controlled nucleation. Simultaneously, Pb^{2+} ions coordinate with non-bridging hydrogen phosphate oxygens, forming stable chemical bonds that anchor the PNCs. The NSs' water-insoluble layered structure provides additional protection against moisture and ion migration. This combined chemical and physical stabilization strategy enhances the structural integrity and long-term optoelectronic performance of the PNCs. The excellent ion absorptivity of $ZrH_2P_2O_8$ was assumed to benefit the nucleation and growth of PNCs on its surface (Figure S1a, Supporting Information). To confirm this, we first investigated the morphology and crystalline nature of $ZrH_2P_2O_8$. White $ZrH_2P_2O_8$ powder exhibits an NS-like morphology, and the absence of sharp peaks in its X-ray diffraction (XRD) spectrum indicates that it is amorphous (Figure S1b, Supporting Information).[26] Scanning electron microscopy (SEM) combined with energy-dispersive spectroscopy (EDS) confirms the presence of all constituent elements in $ZrH_2P_2O_8$ (Figure S1c, Supporting Information). It also has a layered crystal structure and abundant hydroxyl (-OH) groups on its surface (Figure S2a, Supporting Information), which contribute to its strong ion-exchange properties and high absorptivity of Pb^{2+}. Based on these characteristics, we hypothesized that surface ion exchange between FA^+ and H^+ on the surface of $ZrH_2P_2O_8$ would occur readily. To verify Pb^{2+} and FA^+ absorptivity and ion exchange, we immersed $ZrH_2P_2O_8$ in $PbBr_2$/DMF and FAOAc/DMF solutions, respectively, for 24 h, followed by washing. The SEM images and EDS mapping confirmed the presence of Pb^{2+} on the surface of $ZrH_2P_2O_8$ after the ion exchange reaction (Figure S2b, Supporting Information), validating its Pb^{2+} absorptivity. Additionally, the detection of carbon (C) and nitrogen (N) from FA^+ ions on the $ZrH_2P_2O_8$ surface (Figure S2c, Supporting Information) indicates successful ion exchange. These characteristics of $ZrH_2P_2O_8$ prompted us to use it to synthesize various novel halide perovskite composites. In particular, employing phenacyl bromide as the only source of bromide ions in the reaction mixture, we synthesized $FAPbBr_3$, $FAPbBr_{3-x}Cl_x$, and $FAPbBr_{3-x}I_x$ NCs, along with their respective composites. All of the associated reactions are summarized in **Scheme 2**.

$FAPbBr_3@ZrH_2P_2O_8$, $FAPbBr_{3-x}Cl_x@ZrH_2P_2O_8$, and $FAPbBr_{3-x}I_x@ZrH_2P_2O_8$ were synthesized via the hot injection method. An FA oleate stock solution was prepared by initially vacuum-stirring FA acetate and oleic acid (OA) at 120 °C for 10 min, after which it was exposed to a N_2 atmosphere for 90 min at the same temperature, resulting in a clear, yellowish solution. In the synthesis of green-emitting $FAPbBr_3$ NCs, PbO, phenacyl bromide, OA, and 1-octadecene (ODE) were vacuum-stirred at 120 °C for 10 min. The reaction then proceeded under N_2 for 60 min before the temperature was increased to 220 °C. Oleylamine (OAm) was introduced, causing the solution to turn yellow. After annealing and the addition of FA oleate, the reaction was terminated, and NCs were obtained by centrifugation. This three-precursor synthesis method employs phenacyl bromide as the bromide precursor. Initially, formamidinium acetate undergoes a reaction with OA, yielding FA(OOCR) and acetic acid [Step 1]. Simultaneously, OAm, acting as a nucleophile, participates in a nucleophilic substitution reaction by targeting the δ^+ centre (the C attached to Br in phenacyl bromide), resulting in the expulsion of the leaving group and the subsequent generation of HBr [Step 2]. Subsequently, the resultant amine group of the phenacyl bromide derivative undergoes a reaction with OA, leading to the formation of an ionic salt [Step 3]. The generated HBr then reacts with OAm to form oleylammonium bromide, which acts as a source of bromide during the synthesis process [Step 4]. PbO also reacts with an available carboxylic acid group to produce lead acetate [Step 4]. These precursors undergo a final reaction, yielding $FAPbBr_3$ [Step 5]. This mechanism remains consistent for all mixed halides, e.g., $FAPbBr_{3-x}Cl_x$ and $FAPbBr_{3-x}I_x$ NCs.

In our synthetic strategy, phenacyl bromide served as the bromide source, reacting with formamidinium and PbO precursors to form $FAPbBr_3$ NCs with a well-defined stoichiometry. However, when $PbCl_2$ or PbI_2 was introduced to generate Cl/Br (Cl: Br = 0.55: 0.45) or I/Br (I: Br = 0.75: 0.25) mixed-halide NCs, these halide precursors exhibited different reactivities toward phenacyl bromide. Control experiments revealed multiple emission peaks (Figure S3a,b, Supporting Information), indicative of phase segregation. These disparities are attributed to differences in solubility, bonding characteristics, and reaction kinetics, necessitating deviations from theoretical feed ratios to achieve the desired halide composition and phase purity. Due to the varying reactivities, uniform precursor ratios could not be applied across all halide systems, complicating emission control. Through careful optimization of precursor ratios, we were able to suppress phase segregation and obtain single, compositionally uniform emission peaks for each mixed-halide NC. Although phenacyl bromide was the only halide source directly introduced, $PbCl_2$ or PbI_2 were more effectively incorporated under our reaction conditions, suggesting a higher intrinsic reactivity or incorporation efficiency compared to PbO. Based on these findings, we conclude that precursor-specific adjustments beyond stoichiometric predictions are crucial for achieving compositional and optical uniformity in mixed-halide perovskite NCs.

2.2. Structural and Morphological Characterization of the Perovskite Materials

All of the NCs and their composites were structurally characterized using XRD analysis. The XRD pattern for $FAPbX_3$ displays a pure cubic phase (Figure S4a–c, Supporting Information). The diffraction peaks observed at 14.7°, 21°, 29.8°, 33.3°, 37°, 43°, and 45° correspond to the cubic phase of $FAPbBr_3$ NCs. These same peaks were also detected in the $FAPbBr_3@ZrH_2P_2O_8$ composite (Figure S4b, Supporting Information) alongside the characteristic peaks of $ZrH_2P_2O_8$.[27] The XRD patterns for other perovskite composites are present (Figure S4a,c, Supporting

Synthesis scheme for $FAPbBr_3$

Step 1

$$FAOAc + RCOOH \longrightarrow FA(OOCR) + HOAc$$

Step 2

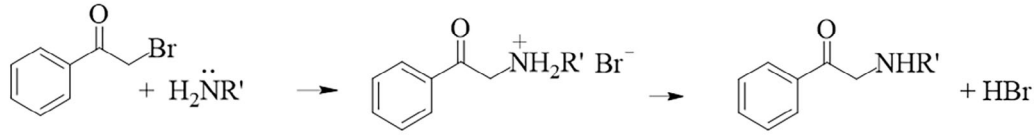

$R'NH_2$ = Oleylamine

Step 3

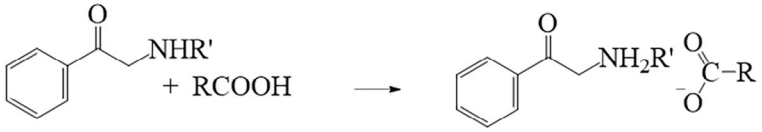

RCOOH = Oleic acid

Step 4

$$PbO + 2RCOOH \longrightarrow Pb(OOCR)_2 + 2H^+$$

$$H^+ + Br^- \longrightarrow HBr$$

$$HBr + R'NH_2 \longrightarrow R'NH_3Br$$

Step 5

$$Pb(OOCR)_2 + FA(OOCR) + 3R'NH_3Br \longrightarrow FAPbBr_3 + 3R'NH_3(OOCR)$$

Synthesis scheme for $FAPbBr_{3-x}Cl_x$

$$PbCl_2 + FA(OOCR) + 3R'NH_3Br \longrightarrow FAPbBr_{3-x}Cl_x + 3R'NH_3(OOCR)$$

Synthesis scheme for $FAPbBr_{3-x}I_x$

$$PbI_2 + FA(OOCR) + 3R'NH_3Br \longrightarrow FAPbBr_{3-x}I_x + 3R'NH_3(OOCR)$$

Scheme 2. Synthesis scheme for $FAPbX_3$ NCs.

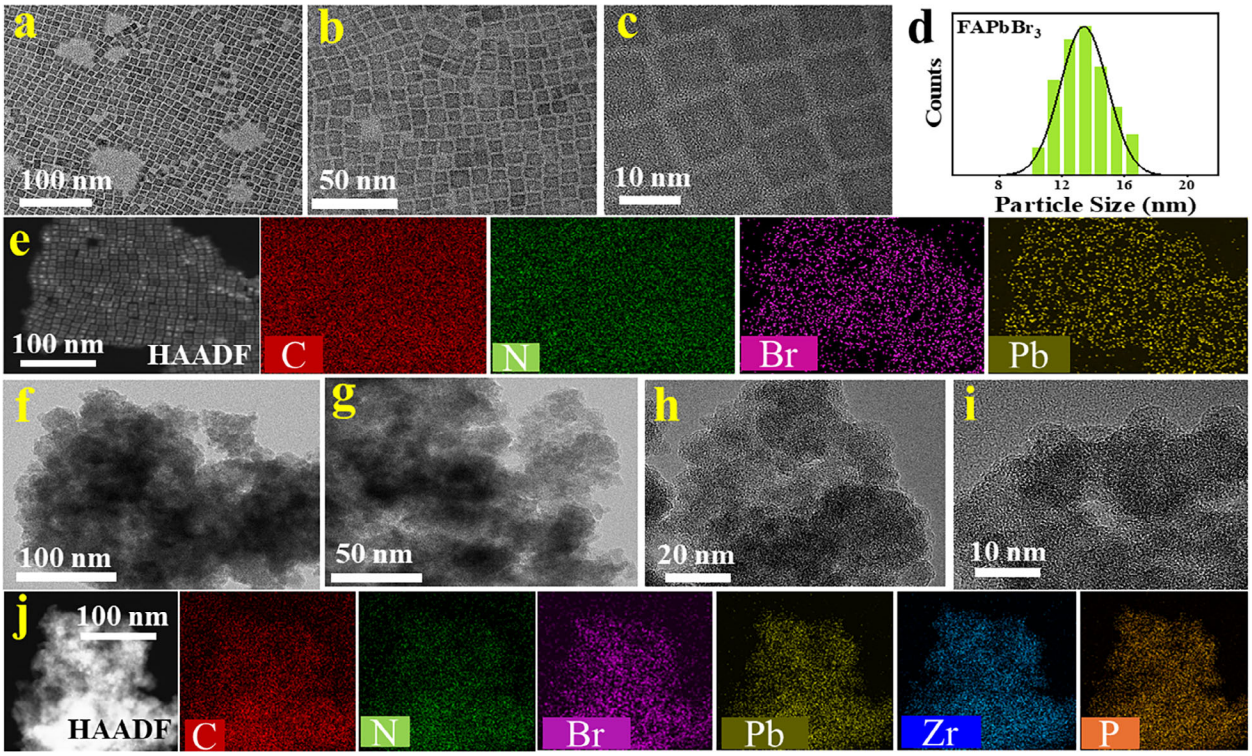

Figure 1. Morphology and elemental composition analyses of pure $FAPbBr_3$ NCs and $FAPbBr_3@ZrH_2P_2O_8$. a–c) TEM images of cube-shaped pure $FAPbBr_3$ NCs at different magnifications. d) Particle size distribution of the NCs obtained from the panel a. e) HAADF image and elemental mapping of $FAPbBr_3$ NCs. f–i) TEM image of cube-shaped $FAPbBr_3@ZrH_2P_2O_8$ at different magnifications. j) HAADF image and elemental mapping of $FAPbBr_3@ZrH_2P_2O_8$.

Information). SEM images and EDS mapping of pure $FAPbX_3$ NCs are present (Figures S5a–S7a, Supporting Information). The EDS mapping demonstrates a homogeneous distribution of the constituent elements in the $FAPbX_3$ NCs. SEM–EDS analysis also confirms the presence of the expected elements in the $FAPbX_3@ZrH_2P_2O_8$, while EDS mapping highlights the uniform distribution of the elements in $FAPbX_3$ NCs across the surface of the $ZrH_2P_2O_8$ NSs (Figure S5b–S7b, Supporting Information). To investigate the morphology of the fabricated materials, we employed transmission electron microscopy (TEM). The TEM images in **Figure** 1a–c depict cubic-shape $FAPbBr_3$ NCs at varying magnifications. The accompanying histogram in Figure 1d presents the size distribution of these NCs, which ranged from ≈10 to 16 nm.[28] The TEM images of $FAPbBr_3@ZrH_2P_2O_8$ displayed in Figure 1f–i depict the amorphous nature of $ZrH_2P_2O_8$ NSs, with the PNCs capped by the amorphous NSs. High-angle annular dark field scanning transmission electron microscopy (HAADF-STEM) images and EDS elemental mapping results for $FAPbBr_3$ NCs and $FAPbBr_3@ZrH_2P_2O_8$ confirm the presence of all of the expected elements inside the pure NCs and $FAPbBr_3@ZrH_2P_2O_8$ composite (Figure 1e,j). Subsequently, TEM imaging was also conducted at various magnifications for pure $FAPbBr_{3-x}Cl_x$, $FAPbBr_{3-x}I_x$ NCs, $FAPbBr_{3-x}Cl_x@ZrH_2P_2O_8$, and $FAPbBr_{3-x}I_x@ZrH_2P_2O_8$ (Figure S8a–d, Supporting Information). TEM images of pure $FAPbBr_{3-x}Cl_x$ and $FAPbBr_{3-x}I_x$ NCs reveal their cubic morphology (Figure S8a,c, Supporting Information), while the corresponding histograms respectively validate the $FAPbBr_{3-x}Cl_x$ and $FAPbBr_{3-x}I_x$ nanocubes, indicating dimensions ranging approximately from 10 to 14 nm and 11 to 15 nm, respectively. TEM images of the $FAPbBr_{3-x}Cl_x@ZrH_2P_2O_8$ and $FAPbBr_{3-x}I_x@ZrH_2P_2O_8$ composites reveal their amorphous nature, with the perovskites encapsulated within amorphous NSs (Figure S8b,d, Supporting Information).

2.3. Surface Chemical Analysis

To confirm the presence of the phenacyl moiety, we conducted nuclear magnetic resonance (NMR) spectroscopy. In phenacyl bromide, a high-intensity peak is observed at 4.40 ppm for the H proton, which is associated with C-bromine, resulting in a slight upfield shift for this proton (Figure S9, Supporting Information). Three different H protons present in the phenyl ring also exhibit peaks at 7.43 ppm (c), 7.55 ppm (d), and 7.92 ppm (b). In $FAPbBr_3$, a highly intense peak appears at 7.21 ppm for the non-deuterated chloroform solvent, while nitrogen-containing C-H exhibits a less-intense peak at 3.83 ppm for OAm. In the aliphatic region, multiple highly intense peaks are observed below 2.3 ppm for ODE, OA, and OAm. Three smaller peaks appear at 7.41 ppm (c), 7.48 ppm (d), and 7.99 ppm (b) for the three types of H protons present in the phenyl ring of phenacyl bromide. These peaks indicate the successful insertion of phenacyl bromide into $FAPbBr_3$ (Figure S9, Supporting Information).[29]

After confirming the presence of the phenacyl moiety, we used X-ray photoelectron spectroscopy (XPS) to investigate the elemental composition, chemical states, and stretching frequencies

of the NCs and composite material. These analyses support the successful incorporation of perovskite NCs inside the $ZrH_2P_2O_8$. The XPS spectra for pure $FAPbBr_3$ NCs contain signals attributed to carbon (C), nitrogen (N), oxygen (O), lead (Pb), and bromine (Br) (Figure S10, Supporting Information), while that for the $FAPbBr_3@ZrH_2P_2O_8$ composite powder suggest that binding energy of C 1s (284, 285, and 286 eV), N 1s (399 and 400 eV), O 1s (530 and 532 eV), Br 3d (67 and 68 eV), and Pb 4f (142 and 138 eV), confirming the presence of $FAPbBr_3$ NCs within the $ZrH_2P_2O_8$ NSs. C 1s peaks at binding energies of 284, 285, and 286 eV were observed for the $FAPbBr_3$ NCs and $FAPbBr_3@ZrH_2P_2O_8$ (Figure S10c, Supporting Information), corresponding to the characteristic bonds of C—C, C—N, and C═N, respectively. The presence of C—N and C═N bonds indicates that the environment was conducive to the formation of FA^+.[30,31] The Br 3d signal exhibits two peaks at 67.88 and 68.05 eV, which are attributed to inner and surface Br^- ions, respectively.[31,32] This reveals the presence of Br^- ions on the surface and in the interior of the $FAPbBr_3$ NCs and $ZrH_2P_2O_8$@ $FAPbBr_3$ composite (Figure S10f, Supporting Information). The XPS signals for Pb 4f in the pure $FAPbBr_3$ and $FAPbBr_3@ZrH_2P_2O_8$ reveal two distinct peaks corresponding to the Pb $4f_{7/2}$ and Pb $4f_{5/2}$ levels (Figure S10g, Supporting Information),[33] while the very small peaks at 135 and 140 eV in both samples are attributed to the presence of Pb (0).[34] The O 1s signals for $FAPbBr_3$ NCs and $FAPbBr_3@ZrH_2P_2O_8$ composite show two peaks for O $1s_{1/2}$ and O $1s_{1/2}$ at 530 and 532 eV, respectively (Figure S10e, Supporting Information), which are consistent with the presence of PbO and organic C═O bonds, respectively.[35] The N 1s signals for $FAPbBr_3$ NCs and $FAPbBr_3@ZrH_2P_2O_8$ have two peaks for N $1s_{1/2}$ and N $1s_{1/2}$ at 399 and 400 eV, indicating the presence of C—NH_3 and C═N respectively (Figure S10d, Supporting Information).[35,36] In the $FAPbBr_3@ZrH_2P_2O_8$ composite (Figure S10h, Supporting Information), the Zr 3d signal contains three peaks at 180, 184, and 187 eV, which are consistent with the presence of Zr—O—C, Zr—O, and Zr—O-P, respectively.[37,38] Detailed XPS analyses of $FAPbBr_3@ ZrH_2P_2O_8$, $FAPbBr_{3-x}Cl_x@ ZrH_2P_2O_8$, and $FAPbBr_{3-x}I_x@ ZrH_2P_2O_8$ are provided in the supporting information (Figures S10,S11, and S12, Supporting Information).

2.4. Optical Properties and Stability

$FAPbBr_3$ NCs synthesized using PbO, FAOAc, and phenacyl bromide exhibit a single sharp green emission peak at 516 nm (**Figure 2**), indicating high crystallinity and uniformity with minimal defects. In contrast, employing $PbBr_2$ and FAOAc as precursors yields $FAPbBr_3$ NCs with three distinct absorption peaks at 493, 466, and 435 nm and three emission peaks at 473, 491, and 524 nm (Figure S13a, Supporting Information), suggesting very low-quality NCs (Figure S13b–d, Supporting Information). This observation verifies our choice of lead and bromine sources in our synthesis strategy. We choose $ZrH_2P_2O_8$ to stabilize PNCs because of its unique layered crystal structure in which the metal atoms are positioned along a plane and bridged by hydrogen phosphate groups. $ZrH_2P_2O_8$ also offers excellent ion-exchange properties and heat stability.[39,40]

The UV-Vis and PL spectra of the synthesized pure NCs and $FAPbX_3@ZrH_2P_2O_8$ samples that varied in their halide content exhibit a single absorbance peak and narrow PL emissions (Figure 2a–d). The UV–vis spectra reveal distinct absorption peaks at 465 nm ($FAPbBr_{3-x}Cl_x$), 513 nm ($FAPbBr_3$), 586 nm ($FAPbBr_{3-x}I_x$), 458 nm ($FAPbBr_{3-x}Cl_x@ZrH_2P_2O_8$), 524 nm ($FAPbBr_3@ZrH_2P_2O_8$), and 613 nm ($FAPbBr_{3-x}I_x@ZrH_2P_2O_8$). The optical bandgap in $FAPbX_3$ NCs and composites is highly sensitive to halide type and ratio, as halide ions significantly influence the electronic band structure. The valence band maximum is primarily formed by halide p orbitals interacting with Pb 6s orbitals, while the conduction band minimum is largely derived from Pb 6p orbitals (Scheme S1, Supporting Information). Halide substitution mainly shifts the valence band, leaving the conduction band relatively stable. Incorporating Cl^-, which has lower-energy p orbitals, shifts the valence band downward, increasing the bandgap and resulting in blue-shifted emission. Replacing Br^- with I^- raises the valence band due to higher-energy 5p orbitals of iodide, narrowing the bandgap and red-shifting emission. In mixed-halide systems, the valence band aligns as a compositional average, enabling smooth bandgap tuning across the visible spectrum. The bandgap determines photon energy via $E=hc/\lambda$, linking higher bandgaps to blue emission and lower ones to red. By adjusting halide content, we achieve precise spectral control, consistent with the previous theoretical and experimental findings.[41]

When stimulated by an excitation wavelength of 350 nm, the samples manifest symmetric PL emission peaks at 475 nm ($FAPbBr_{3-x}Cl_x$), 542 nm ($FAPbBr_3$), 618 nm ($FAPbBr_{3-x}I_x$), 470 nm ($FAPbBr_{3-x}Cl_x@ZrH_2P_2O_8$), 535 nm ($FAPbBr_3@ZrH_2P_2O_8$), and 617 nm ($FAPbBr_{3-x}I_x@ZrH_2P_2O_8$). These emission profiles are accompanied by narrow full width at half maximum (FWHM) values of 19 nm ($FAPbBr_{3-x}Cl_x$), 20 nm ($FAPbBr_3$), 30 nm ($FAPbBr_{3-x}I_x$), 18 nm ($FAPbBr_{3-x}Cl_x@ZrH_2P_2O_8$), 21 nm ($FAPbBr_3@ZrH_2P_2O_8$), and 35 nm ($FAPbBr_{3-x}I_x@ZrH_2P_2O_8$) (Figure 2c,d). A slight Stokes shift of 10.4, 29.0, and 31.4 nm is observed for $FAPbBr_{3-x}Cl_x$, $FAPbBr_3$, and $FAPbBr_{3-x}I_x$, respectively. In contrast, the Stokes shift for the corresponding composites $FAPbBr_{3-x}Cl_x@ZrH_2P_2O_8$, $FAPbBr_3@ZrH_2P_2O_8$, and $FAPbBr_{3-x}I_x@ZrH_2P_2O_8$ was reduced to 4.4, 11.6, and 12.0 nm, respectively. This reduction in the Stokes shift indicates the effective removal of trap states due to the encapsulation of the perovskite within $ZrH_2P_2O_8$. These observations verify the refined optical properties and structural homogeneity of the materials, reflecting a high degree of precision in their photo-physical characteristics.

The PL QY and stability of $FAPbBr_3$, $FAPbBr_{3-x}Cl_x$, and $FAPbBr_{3-x}I_x$ NCs increased after adding $ZrH_2P_2O_8$. In particular, the PL QY for $FAPbBr_{3-x}Cl_x@ZrH_2P_2O_8$, $FAPbBr_3@ZrH_2P_2O_8$, and $FAPbBr_{3-x}I_x@ZrH_2P_2O_8$ composites are 41%, 88.57%, and 38%, respectively (Table S1, Supporting Information). This considerable increase in the PL QY results from hydrogen phosphate removing trap states by binding oxygen to Pb. $FAPbX_3$ NCs are prone to degradation following exposure to moisture and tend to aggregate at high temperatures, which is a significant concern for their use in optoelectronic applications. Therefore, we monitored the stability of the $FAPbX_3$ NCs and the $FAPbBr_{3-x}Cl_x@ZrH_2P_2O_8$, $FAPbBr_3@ZrH_2P_2O_8$, and

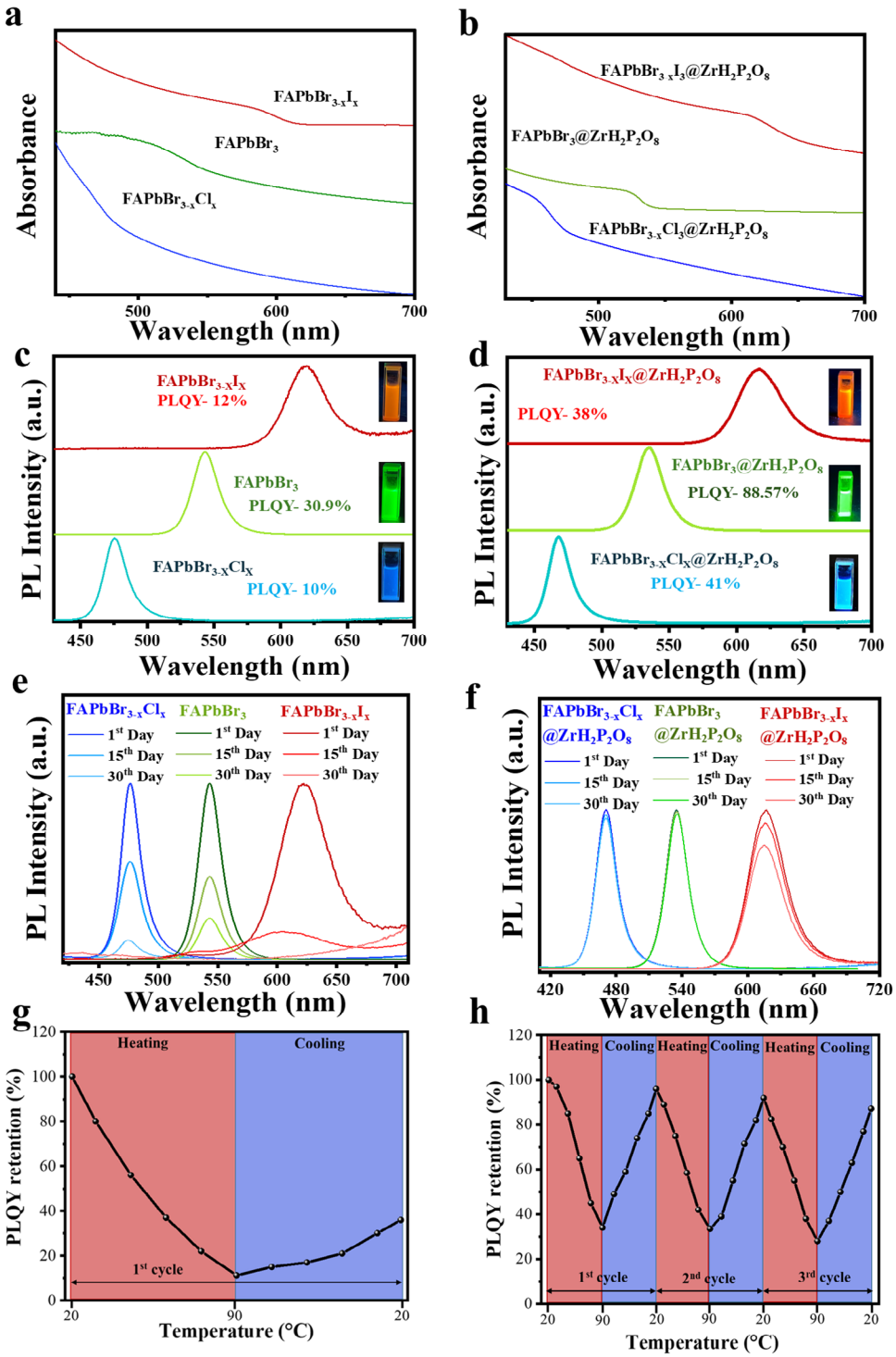

Figure 2. Phototoluminescence properties of $FAPbX_3@ZrH_2P_2O_8$ composites. a) Absorbance for $FAPbX_3$ NCs. b) Absorbance for $FAPbX_3@ZrH_2P_2O_8$ composites. c) PL spectra for pure $FAPbX_3$. d) PL spectra for $FAPbX_3@ZrH_2P_2O_8$. e) Humidity stability of $FAPbX_3$ NCs over 30 days. f) Humidity stability of $FAPbX_3@ZrH_2P_2O_8$ composites over 30 days. g) PL retention curves for $FAPbBr_3$ NCs during repeated heating–cooling cycles. h) PL retention curves for $FAPbBr_3@ZrH_2P_2O_8$ composites during repeated heating–cooling cycles in which the temperature was raised from 20 to 90 °C and then reduced from 90 to 0 °C.

$FAPbBr_{3-x}I_x@ZrH_2P_2O_8$ composites 30 days of exposure to a humid environment, with the composites exhibiting much higher stability than the pure NCs (Figure 2e,f, respectively). The stability assessment of $FAPbX_3$ NCs is delineated (Figure 2e), revealing a pronounced deficiency in stability. Contrastingly, the integration of $FAPbX_3@ZrH_2P_2O_8$ composite materials, as depicted in Figure 2f, showcases notably superior stability. In particular, the PL intensity of $FAPbBr_{3-x}Cl_x@ZrH_2P_2O_8$, $FAPbBr_3@ZrH_2P_2O_8$, and $FAPbBr_{3-x}I_x@ZrH_2P_2O_8$ decline by only 7%, 8% and 12%, respectively, relative totheir initial levels, whereas the pure $FAPbX_3$ NCs experienced a rapid decrease in PL intensity within 15 days. The composites also produced fluorescence under UV light even after one year of exposure to humidity and an image of the composite dissolved in toluene after one year of exposure to humidity under UV light (365 nm) is also presented (Figure S14, Supporting Information). The considerable improvement in stability in a humid environment demonstrated by the $FAPbX_3@ZrH_2P_2O_8$ composites highlights the benefits derived from amorphous $FAPbX_3$ NSs as a stabilizing agent. The chemical interactions between $ZrH_2P_2O_8$ NSs and $FAPbX_3$ perovskite NCs play a central role in enhancing material stability. Specifically, FA^+ ions undergo ion exchange with protons on the hydrogen phosphate groups of $ZrH_2P_2O_8$:

$$ZrH_2P_2O_8 - PO_4H + FA^+ \rightarrow ZrH_2P_2O_8 - PO_4FA + H^+ \quad (1)$$

This reaction enriches the local FA^+ concentration at the surface, promoting controlled, heterogeneous nucleation of $FAPbX_3$. Simultaneously, Pb^{2+} ions coordinate with non-bridging hydrogen phosphate oxygen atoms (P═O) on the NSs:

$$ZrH_2P_2O_8 - P=O + Pb^{2+} \rightarrow ZrH_2P_2O_8 - P=O\cdots Pb^{2+} \quad (2)$$

The large 2D $ZrH_2P_2O_8$ NSs possess a robust, layered structure that is water-insoluble, thereby protecting the PNCs from moisture and environmental degradation. The PNCs are chemically bonded to the NSs through interactions between lead ions (Pb^{2+}) and oxygen atoms, which help stabilize the surface and suppress ion migration. This synergy of chemical bonding and physical encapsulation effectively mitigates halide loss, ionic movement, and moisture-induced degradation.

The $FAPbBr_3@ZrH_2P_2O_8$ composite had a PL QY of 88.57%, which was higher than the other composites. $FAPbBr_3@ZrH_2P_2O_8$ also has stronger photo-stability, with a PL intensity retention of 95% after 35 h of light irradiation (Figure S15, Supporting Information).

The outstanding photo-stability stems from the multifaceted protective role of the $ZrH_2P_2O_8$ NS encapsulation. Acting as a robust physical barrier, the 2D $ZrH_2P_2O_8$ layer effectively shields perovskite NCs from common degradation triggers such as moisture, oxygen, and high-energy photons. In addition to this physical protection, $ZrH_2P_2O_8$ also provides chemical passivation: its hydrogen phosphate groups coordinate with undercoordinated Pb^{2+} sites, reducing trap states and inhibiting light-induced defect formation. Furthermore, the inorganic lattice of $ZrH_2P_2O_8$ exhibits low phonon energy, which minimizes local thermal vibrations and reduces heat accumulation during irradiation, mitigating thermally induced degradation. The NS encapsulation also serves as an effective oxygen diffusion barrier, restricting access of reactive oxygen species, particularly superoxide radicals, to the excited perovskite surface, thereby preventing oxygen-driven decomposition pathways (Table S2, Supporting Information).

The observed PL spectra, which consistently centered ≈534 nm for various excitation wavelengths, indicate a uniform particle size distribution within the synthesized composite. The thermal stability of the composite powder is also found to be high,[42,43] with successive cycles of heating and cooling (from 20 °C to 90 °C and back to 20 °C), producing a consistent decrease in the PL intensity with an increase in the temperature. Remarkably, after 10 consecutive cycles, the PL intensity rebounds, demonstrating a recovery of over 90% of its initial value (Figure 2h). In contrast, with the pure $FAPbBr_3$ NCs, the PL intensity decreases dramatically after one cycle (Figure 2g).

2.5. Induction of Chirality, Morphological Analysis, and Surface Chemical Composition of Chiral Perovskites

Though the synthesized composites exhibit excellent stability and PL QYs, they are not CPL active. Therefore, to induce chirality, we introduced a chiral moiety to the perovskite composite. Colloidal PNCs with chiral ligands have significant potential for use in CPL applications due to their high PL efficiency, spin-orbit coupling (SOC), and flexibility in terms of composition and ligand choice. However, ensuring consistent and controllable polarized light emissions remains a challenge. To resolve this, we developed cellulose-encapsulated perovskite materials with promising chiroptical properties. Strong electronic coupling between the cellulose and perovskite composites facilitates CPL both in solution and solid-state. SEM images and EDS mapping of cellulose are presented (Figure 4b–d; Figure S16, Supporting Information, respectively). To verify the incorporation of perovskite NCs within the cellulose matrix, we conducted a sedimentation experiment comparing three samples dispersed in toluene: i) pure $FAPbX_3$, ii) $FAPbX_3@ZrH_2P_2O_8$, and iii) $FAPbX_3@ZrH_2P_2O_8$@cellulose (Figure S17a–c, Supporting Information). While all samples initially formed homogeneous dispersions, the cellulose-containing composite underwent rapid sedimentation, becoming optically clear within 40 min. This rapid phase separation, accompanied by clear supernatant under UV illumination, reflects strong interaction and integration between the PNCs and the cellulose matrix. In contrast, the $ZrH_2P_2O_8$ stabilized composite required nearly 1 h to settle, and the pristine $FAPbX_3$ remained largely suspended. These observations support the robust physical anchoring of PNCs within the cellulose network. Moreover, the $FAPbX_3@ZrH_2P_2O_8$@cellulose sample exhibited a more rapid decrease in PL intensity, indicating a pronounced interaction between cellulose and the perovskite–inorganic hybrid composite (Figure S17d).

We then conducted Fourier-transform infrared (FTIR) spectroscopy analysis of the $FAPbBr_{3-x}Cl_x@ZrH_2P_2O_8$, $FAPbBr_3@ZrH_2P_2O_8$, and $FAPbBr_{3-x}I_x@ZrH_2P_2O_8$ composites and their cellulose-encapsulated counterparts (Figure S18a–c, Supporting Information). In the FTIR spectra, a prominent peak at 989 cm^{-1} indicates the P-O stretching vibrations characteristic of the interlayer PO_4 group, while the FTIR peaks

at 2922 and 2856 cm^{-1} and the peak at 1445 cm^{-1} correspond to the stretching and bending modes, respectively, of hydrocarbon groups. The FTIR peak observed at 1715 cm^{-1} is also attributed to C═N symmetric stretching, which indicates the formation of FA^+. The peak observed at 1544 cm^{-1} is attributed to the C–N stretching mode, while the peaks at 1639 and 1458 cm^{-1} are ascribed to carboxylic groups, suggesting the presence of OA.[44–46] Additionally, the peak at ≈3600 cm^{-1} indicates the presence of hydroxyl groups in both the cellulose and $FAPbX_3@ZrH_2P_2O_8$@cellulose.[47,48] However, this peak is notably absent for the $FAPbX_3@ZrH_2P_2O_8$ composite, confirming the presence of cellulose in the cellulose-encapsulated perovskite composite. Furthermore, XPS analyses of $FAPbX_3@ZrH_2P_2O_8$ and $FAPbX_3@ZrH_2P_2O_8$@cellulose materials were carried out to show successful incorporation of cellulose inside perovskite composite material (Figure S19a–c, Supporting Information). Br and Cl spectra show that Br 3d peaks at 67.1 and 68.1 eV and Cl 2p peaks at 196.8 and 198.46 eV for $FAPbBr_{3-x}Cl_x@ZrH_2P_2O_8$ shift slightly to 67.0 and 68.2 and 196.5 and 198.6 eV, respectively, after cellulose incorporation, accompanied by noticeable peak broadening. This suggests changes in the halide coordination environment and increased surface heterogeneity due to hydrogen bonding within the chiral cellulose matrix. Pb 4f peaks shift from 137.3 and 142.2 eV to 137.2 and 142.1 eV, along with significant peak broadening and disappearance of satellite features for $FAPbBr_{3-x}Cl_x@ZrH_2P_2O_8$@cellulose, indicating reduced surface defects and stronger interaction with cellulose hydroxyl groups. Zr 3d peaks shift from 181.18, 184.2, and 187.2 eV to 181.3, 183.3, and 188.9 eV, reflecting modified bonding environments possibly due to coordination with cellulose. These shifts and spectral changes across all elements in $FAPbBr_{3-x}Cl_x@ZrH_2P_2O_8$@cellulose material confirm effective integration of the perovskite composite into the cellulose matrix through non-covalent interactions and enhanced surface passivation. Detailed information for $FAPbBr_3@ZrH_2P_2O_8$@cellulose and $FAPbBr_{3-x}I_x@ZrH_2P_2O_8$@cellulose is explained in the Supporting Information.

2.6. Demonstration of the Chiroptical Properties of the Chiral Perovskite

Perovskites are inherently achiral, so the chiroptical activity in our cellulose-based composites does not result from direct coordination of individual glucose units to the perovskite surface. While glucose monomers have intrinsic molecular chirality, their linear polymerization into cellulose chains alone does not produce macroscopic chirality.[49] Instead, chirality arises from the hierarchical supramolecular assembly of these chains into helically twisted microfibrils that bundle into larger macrofibers, forming a rigid, chiral scaffold.[50] This architecture is stabilized by extensive intra- and intermolecular hydrogen bonding among the hydroxyl groups of cellulose (Figure 4a). When $ZrH_2P_2O_8$ stabilized PNCs are incorporated, they interact through hydrogen bonding, hydrophobic contacts with surface ligands such as oleic acid and oleylamine, and coordination between Pb^{2+} ions and cellulose hydroxyl groups.[51,52] Although the glucose units are covalently bound within the cellulose, their hydroxyl groups remain chemically accessible to help stabilize the interface, while the primary chirality transfer is governed by the supramolecular helicity of the cellulose fibers acting as a chiral scaffold.

After encapsulating the chiral moiety, we measured the circular dichroism (CD) and CPL of $FAPbBr_{3-x}Cl_x@ZrH_2P_2O_8$, $FAPbBr_3@ZrH_2P_2O_8$, and $FAPbBr_{3-x}I_x@ZrH_2P_2O_8$ in solution and solid-state. CD provides insights into the structural properties of the ground electronic state of a system, while CPL reveals the structural characteristics of its luminescent excited state.[53] Cellulose results in the generation of CD signals due to the presence of chiral units. Cellulose only has a broad negative CD signal with maximum intensity at 332 nm in solid and solution, and does not produce any significant CPL signal (Figure S20a,b, Supporting Information). Similarly, $FAPbBr_{3-x}Cl_x@ZrH_2P_2O_8$, $FAPbBr_3@ZrH_2P_2O_8$, and $FAPbBr_{3-x}I_x@ZrH_2P_2O_8$ do not exhibit any CPL signals as expected due to the absence of chiral ligands or a chiral matrix (Figure S21a–c, Supporting Information).

We measured the PL, UV, and CD spectra for our composites in solution and solid-state (**Figure 3**; Figure S22a–c, Supporting Information). Strong CD broad signals are observed for $FAPbBr_{3-x}Cl_x@ZrH_2P_2O_8$@cellulose, $FAPbBr_3@ZrH_2P_2O_8$@cellulose, and $FAPbBr_{3-x}I_x@ZrH_2P_2O_8$@cellulose in solution and solid-state at a range of 300–600, 400–650, and 400-710 nm, respectively (Figure 3d–i). The characteristic CD peak at 332 nm of pure cellulose is also present in all these composite materials. However, this feature is less prominent in solid-state materials due to its significantly reduced intensity. This indicates the new CD signals in all composites appear due to the cellulose-induced chirality. The new induced CD signals in composites are associated with absorption peaks of the corresponding composite materials. This correlation occurs because CD spectra are recorded in the absorption region, as CD measures the differential absorption of left- and right-circularly polarized light by chiral composite systems during electronic transitions, which only take place at wavelengths where these materials absorb light. The differences between the CD spectra of pure cellulose and cellulose-perovskite composites stem from multiple factors beyond simple chirality transfer.[54] While cellulose's intrinsic chiroptical activity arises from its helically twisted fibrillar structure, intrinsically directed by the molecular chirality of its glucose units, embedding $FAPbX_3$ NCs stabilized with $ZrH_2P_2O_8$ introduces additional asymmetry through non-covalent interactions such as hydrogen bonding and hydrophobic contacts between surface ligands and cellulose chains. The $ZrH_2P_2O_8$ NSs further strengthen this effect by forming hydrogen bonds with cellulose, bringing the perovskite ligand interface into closer contact with the chiral matrix and enhancing mirror-symmetry breaking. This is further modulated by halide-dependent tuning of the perovskite's band structure and excitonic properties. This composite formation induces local reorganization within the cellulose network, altering hydrogen bonding and chain conformation, which modifies ground-state electronic interactions and shapes the CD response. Also, the solution-phase composite displays pronounced humps and fine structure due to greater conformational flexibility, whereas the solid-state spectra are broader and less structured because of tighter molecular packing.

The corresponding ultraviolet absorption spectra were not obtained directly from the CD instrument. In systems where NCs

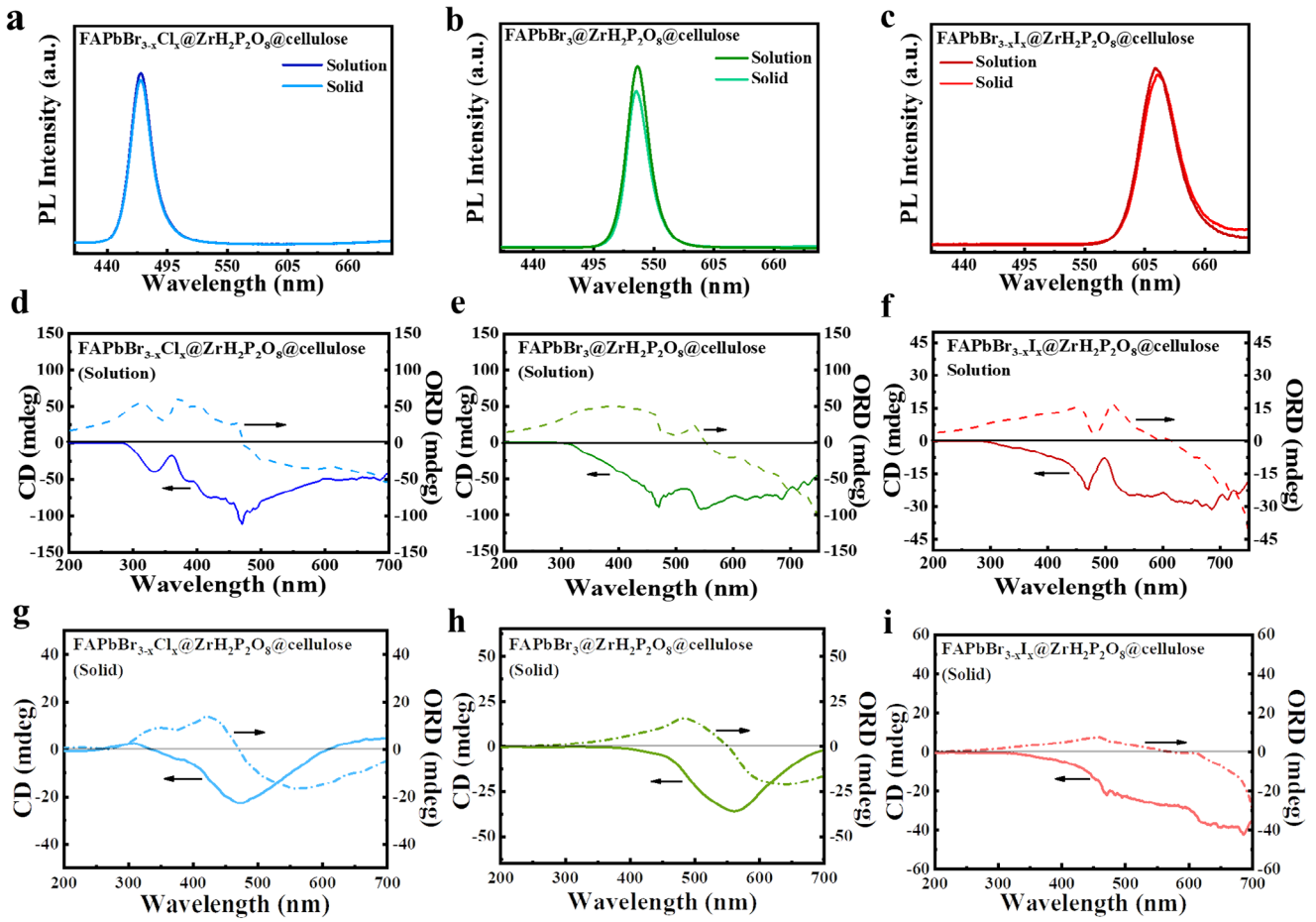

Figure 3. Chiroptical properties of $FAPbX_3$@$ZrH_2P_2O_8$@cellulose in solution and solid-state. a) PL of $FAPbBr_{3-x}Cl_x$@$ZrH_2P_2O_8$@cellulose. b) PL of $FAPbBr_3$@$ZrH_2P_2O_8$@cellulose. c) PL of $FAPbBr_{3-x}I_x$@$ZrH_2P_2O_8$@cellulose. d) CD and ORD for $FAPbBr_{3-x}Cl_x$@$ZrH_2P_2O_8$@cellulose in solution. e) CD and ORD for $FAPbBr_3$@$ZrH_2P_2O_8$@cellulose in solution. f) CD and ORD for $FAPbBr_{3-x}I_x$@$ZrH_2P_2O_8$@cellulose in solution. g) CD and ORD for $FAPbBr_{3-x}Cl_x$@$ZrH_2P_2O_8$@cellulose in the solid-state. h) CD and ORD for $FAPbBr_3$@$ZrH_2P_2O_8$@cellulose in the solid-state. i) CD and ORD for $FAPbBr_{3-x}I_x$@$ZrH_2P_2O_8$@cellulose in the solid-state.

are embedded in optically active polymer matrices such as cellulose, it is common for absorbance spectra acquired during CD measurements to appear noisy due to strong light scattering, high baseline absorbance from the matrix, and broad electronic transitions. This effect, known as absorption flattening, is well documented for turbid or aggregated samples.[55] In our system, the presence of insoluble $ZrH_2P_2O_8$ and fibrous cellulose further increases turbidity, leading to distortions in the CD instrument's absorbance baseline. To address this, we have provided independently measured UV–vis spectra using a conventional spectrophotometer, which is better suited to handle scattering and confirms that the absorption peaks are consistent in both solution and solid-state (Figure S22, Supporting Information).

The optical rotatory dispersion (ORD) of $FAPbBr_{3-x}Cl_x$@$ZrH_2P_2O_8$@cellulose, $FAPbBr_3$@$ZrH_2P_2O_8$@cellulose, and $FAPbBr_{3-x}I_x$@$ZrH_2P_2O_8$@cellulose in solution and solid-state intersects zero rotation at 471, 551, and 616 nm, respectively, which indicates a transition in the chiral properties of the material, possibly related to electronic transitions or changes in the optical activity at this specific wavelength (Figure 3d–i).[56,57] This phenomenon signifies a reversal in the direction and polarity of the rotation of plane-polarized light at these specific wavelengths, illustrating the relationship between the CD and ORD spectra and providing insights into the chiral interactions within the system. Furthermore, we investigated the asymmetry factor (g_{abs}) in these composites. The asymmetry factor (g_{abs}) quantifies the optical activity of a chiral material by measuring the difference in absorbance between left- and right-handed circularly polarized light as follows:

$$g_{abs} = \frac{2 \times (A_R - A_L)}{(A_R + A_L)} \quad (3)$$

where A_L and A_R are the absorbance of left- and right-handed CPL, respectively from the point of view of the receiver. For $FAPbBr_{3-x}Cl_x$@$ZrH_2P_2O_8$@cellulose, $FAPbBr_3$@$ZrH_2P_2O_8$@cellulose, and $FAPbBr_{3-x}I_x$@$ZrH_2P_2O_8$@cellulose in solution, g_{abs} values are –0.017, –0.0145, and –0.0054, respectively, and in the solid-state, g_{abs} values are -2.4×10^{-4}, -2.6×10^{-4}, and -5.2×10^{-3}, respectively (Figure S23a–f, Supporting Information). The

observed reduction in g_{abs} values in the solid-state relative to the solution primarily results from the inherent optical and structural limitations of the solid matrix. In solution, the material is well-dispersed, enabling efficient interaction with circularly polarized light and resulting in stronger CD signals. In contrast, the solid-state environment imposes optical constraints such as dense packing, reduced accessibility of NCs, and increased scattering from matrix components like cellulose and $ZrH_2P_2O_8$. Solid-state samples are also prone to light scattering, baseline distortion, and interface reflection, which can obscure or flatten the fine spectral features needed for accurate CD measurements. These effects lower the number of optically active centers, decreasing CD intensity while absorbance remains relatively unchanged, thus suppressing g_{abs}. This behavior is consistent with the commonly observed reduction in PL quantum yield in the solid-state, where physical constraints limit optical efficiency.[58]

The homogeneous grafting of the perovskite composites onto the cellulose fibre substrate is successfully achieved (**Figure 4a**), as confirmed by the accompanying SEM images in Figure 4b–d. A CPL response is thus successfully achieved by combining $FAPbX_3@ZrH_2P_2O_8$ with a chiral polymer (**Figure 5a**). The CPL spectra for $FAPbBr_{3-x}Cl_x@ZrH_2P_2O_8$@cellulose, $FAPbBr_3@ZrH_2P_2O_8$@cellulose, and $FAPbBr_{3-x}I_x@ZrH_2P_2O_8$@cellulose were measured in solution and solid-state (Figure 5b–d). Positive CPL signals are observed under excitation at 350 nm in solution, indicating that right-handed CPL is emitted by the cellulose-encapsulated perovskite composites, while negative CPL signals are observed in the solid-state, indicating that left-handed CPL is emitted by these composites. The CPL emission peaks for $FAPbBr_{3-x}Cl_x@ZrH_2P_2O_8$@cellulose, $FAPbBr_3@ZrH_2P_2O_8$@cellulose, and $FAPbBr_{3-x}I_x@ZrH_2P_2O_8$@cellulose in solution are located at 471, 530, and 591, respectively, while they are found at 469, 526, and 601 nm, respectively, in the solid-state (Figure 5b–d). In our system, chirality is transferred to achiral $FAPbX_3@ZrH_2P_2O_8$ nanocomposites by embedding them within a chiral cellulose matrix. The cellulose adopts a helical conformation due to intra- and intermolecular hydrogen bonding, forming a network of non-covalent interactions that governs chirality transfer. After incorporating $ZrH_2P_2O_8$, oleic acid, and oleylamine ligands on the perovskite surface remain partially exposed. Their hydrophobic alkyl chains interact with nonpolar domains of cellulose, while hydroxyl groups in cellulose form hydrogen bonds with Pb^{2+} on the perovskite surface and coordinate with hydrogen phosphate groups in $ZrH_2P_2O_8$. These interactions anchor the chiral polymer matrix close to the NC interface and maintain the helical conformation. This supramolecular assembly establishes a chiral field that induces both CD and CPL. Notably, CD signals retain the same sign in both solution and solid phases, whereas CPL signals exhibit mirror image inversion, right-handed emission in solution and left-handed emission in the solid-state. This divergence stems from the fundamental difference between CD and CPL: CD reflects ground-state chirality, while CPL arises from excited-state chirality governed by transition dipole alignment and coupling. In the solution phase, solvent molecules such as toluene penetrate the composite and disrupt hydrogen bonding within the cellulose, allowing flexible local rearrangements of the supramolecular environment and ligand shell. This reorganization facilitates a chiral excited-state geometry that favors right-handed emission. In contrast, the solid-state environment preserves the intact hydrogen-bonded network of cellulose, restricting conformational freedom and locking the excited-state configuration into an alternative geometry that results in left-handed emission. The consistency of CD sign across both phases confirms the preservation of ground-state chiral environment. Pure cellulose also exhibits same handedness CD peaks in both solution and solid (Figure S20a, Supporting Information). However, subtle spectral shape changes observed in the CD profiles suggest minor differences in local packing and excitonic interactions. These rearrangements are sufficient to invert CPL handedness without altering the ground-state chirality. Additionally, more pronounced vibronic or excitonic features appear in the solution-phase CD spectrum, such as spectral shoulders or fine structure due to enhanced molecular flexibility. In the solid-state, these features are broadened or suppressed owing to constrained dynamics and tighter packing. Collectively, these results highlight the critical role of non-covalent interactions particularly hydrogen bonding and hydrophobic association between cellulose and ligand-coated NCs in establishing a dynamic yet robust chiral environment. This environment responds sensitively to external stimuli such as solvent polarity and phase state, resulting in reversible modulation of excited-state chirality and mirror-image CPL.[59] For $FAPbBr_{3-x}Cl_x@ZrH_2P_2O_8$@cellulose, $FAPbBr_3@ZrH_2P_2O_8$@cellulose, and $FAPbBr_{3-x}I_x@ZrH_2P_2O_8$@cellulose, the ORD spectra exhibit zero rotation crossing points at ≈469, 527, and 611 nm, respectively, in solution and at ≈471, 529, and 614 nm, respectively, in solid form, again indicating a transition in the chiral properties of the material, possibly related to electronic transitions or changes in the optical activity at this specific wavelength (Figure 5e–g). The long-term stability of $FAPbX_3@ZrH_2P_2O_8$@cellulose composite is evaluated under ambient conditions over a period of 30 days. As shown in Figure S24a–c (Supporting Information), all three composite systems $FAPbCl_{3-x}Br_x@ZrH_2P_2O_8$@cellulose, $FAPbBr_3@ZrH_2P_2O_8$@cellulose, and $FAPbI_{3-x}Br_x@ZrH_2P_2O_8$@cellulose retained a substantial portion of their initial photoluminescence intensity. This result indicates that the encapsulation strategy using ZrH_2P_2O NSs and cellulose matrix provides effective stabilization of the perovskite NCs under ambient conditions.

The g_{lum} is a parameter used to quantify the degree of circular polarization of emitted light from a luminescent material.

This notable rotation indicates an excellent g_{lum}, which reflects the degree of emission asymmetry for left and right-handed CPL. g_{lum} is calculated as follows:

$$g_{lum} = \frac{I_R - I_L}{2 \times (I_R + I_L)} \tag{4}$$

where I_R is the intensity of right-handed CPL and I_L is the intensity of left-handed CPL from the perspective of the receiver.

For $FAPbBr_{3-x}Cl_x@ZrH_2P_2O_8$@cellulose, $FAPbBr_3@ZrH_2P_2O_8$@cellulose, and $FAPbBr_{3-x}I_x@ZrH_2P_2O_8$@cellulose in solution, g_{lum} values are 3×10^{-3}, 5.1×10^{-3}, and 5.4×10^{-3}, respectively, and in the solid-state, g_{lum} values are 1.3×10^{-3},

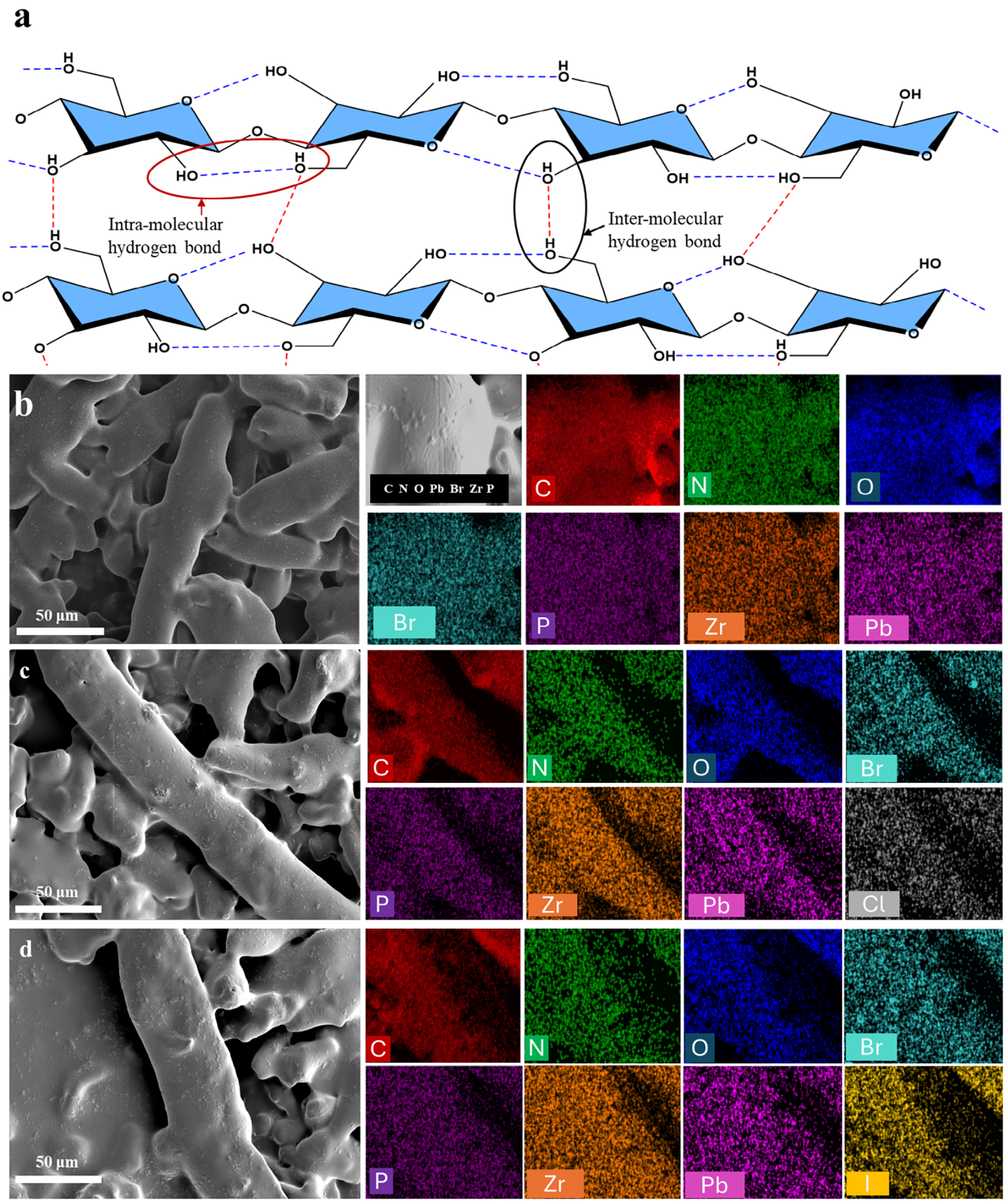

Figure 4. Chemical structure of cellulose polymer and surface analysis of $FAPbX_3$@$ZrH_2P_2O_8$@cellulose. a) Intra- and inter-molecular hydrogen bonds within cellulose. b) SEM image and EDS mapping of the elements in the $FAPbBr_3$@$ZrH_2P_2O_8$@cellulose composite. c) SEM image and EDS mapping of the elements in the $FAPbBr_{3-x}Cl_x$@$ZrH_2P_2O_8$@cellulose composite. d) SEM image and EDS mapping of the elements in the $FAPbBr_{3-x}I_x$@$ZrH_2P_2O_8$@cellulose composite.

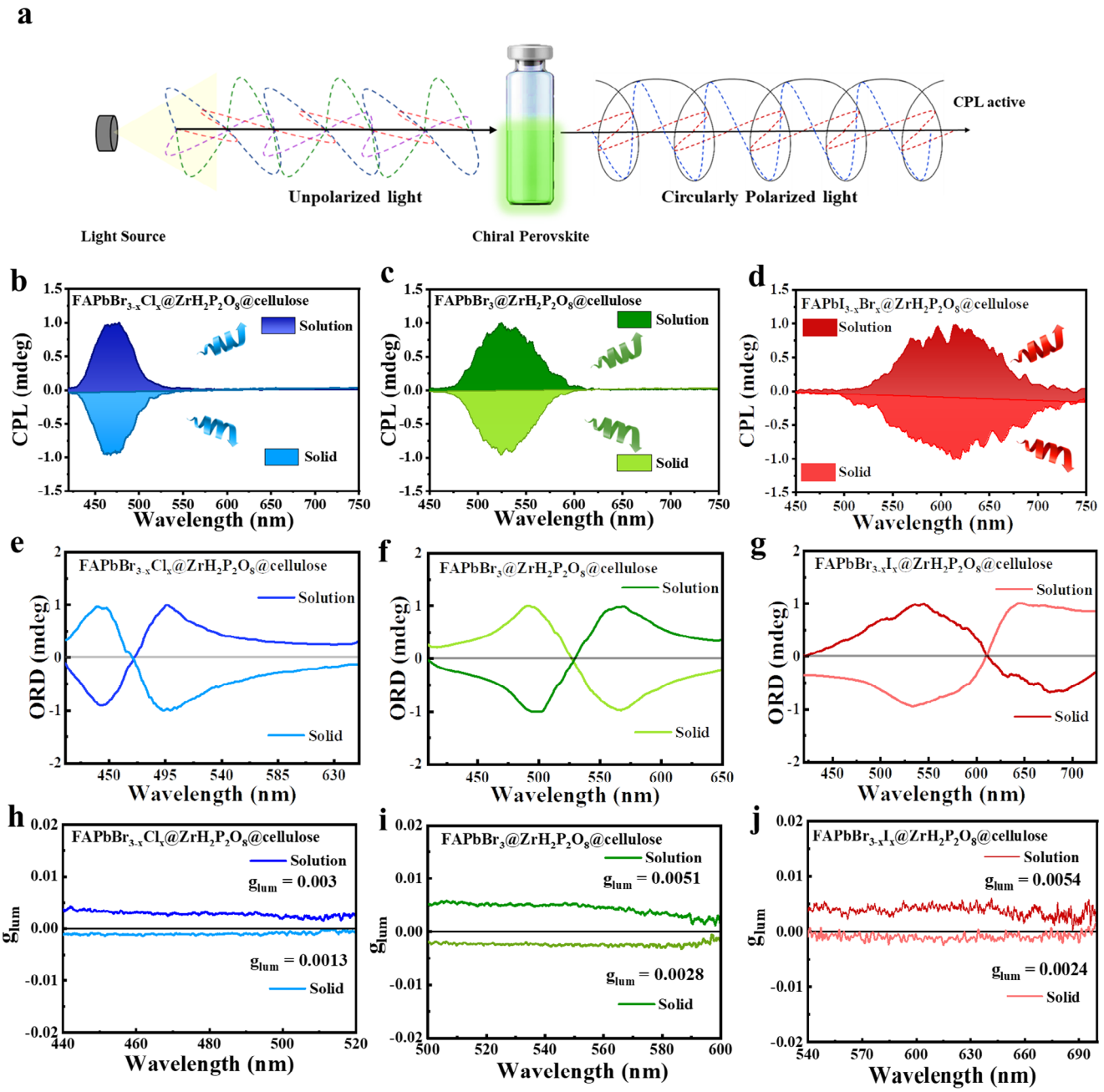

Figure 5. Chiroptical properties of $FAPbX_3@ZrH_2P_2O_8$@cellulose composites in solution and solid-state. a) Schematic diagram of CPL generation from chiral perovskite. b) CPL data for $FAPbBr_{3-x}Cl_x@ZrH_2P_2O_8$@cellulose. c) CPL data for $FAPbBr_3@ZrH_2P_2O_8$@cellulose. d) CPL data for $FAPbBr_{3-x}I_x@ZrH_2P_2O_8$@cellulose. e) ORD data for $FAPbBr_{3-x}Cl_x@ZrH_2P_2O_8$@cellulose. f) ORD data for $FAPbBr_3@ZrH_2P_2O_8$@cellulose. g) ORD data for $FAPbBr_{3-x}I_x@ZrH_2P_2O_8$@cellulose. h) g_{lum} data for $FAPbBr_{3-x}Cl_x@ZrH_2P_2O_8$@cellulose. i) g_{lum} data for $FAPbBr_3@ZrH_2P_2O_8$@cellulose. j) g_{lum} data for $FAPbBr_{3-x}I_x@ZrH_2P_2O_8$@cellulose.

2.8×10^{-3} and 2.4×10^{-3}, respectively (Figure 5h–j). The reduced g_{lum} in the solid-state arises from restricted dipole mobility and steric hindrance within the cellulose framework, compounded by optical losses such as scattering and reabsorption. These environmental constraints diminish chiral emission efficiency without altering the intrinsic chirality of the composite.[60]

The observed CPL inversion and g_{abs} suppression thus highlight the role of supramolecular architecture and excited-state reorganization in dictating chiral emission. Rather than focusing solely on maximizing g_{lum} values, our work provides new insight into chirality transfer mechanisms and stabilization strategies in perovskite-based chiroptoelectronics. This understanding lays the foundation for the future development of tunable, robust, and environmentally stable CPL materials.

While the g_{lum} values observed in this study are moderate compared to systems employing covalently bound chiral ligands, they

reflect a unique strategy that emphasizes excited-state chirality modulation, long-term stability, and environmentally benign processing. A comparative summary of g_{lum} values from representative chiral perovskite systems is provided in Table S3 (Supporting Information).

Collectively, the characterization results indicate that we successfully developed a novel process in which perovskites were deliberately combined with helical cellulose fibers to produce CPL properties. Cellulose is a polysaccharide with the formula $(C_6H_{10}O_5)_n$ that consists of a linear chain of several hundred to many thousands of β (1→4) linked D-glucose units. Due to this structure, cellulose is a chiral polymer. It has the structural flexibility to produce different types of helix with both intramolecular and intermolecular H-bonding (Figure 4a). The interaction between the glucose units in each cellulose polymeric chain may also create different helix structures in solution and solid-state. We observe that $FAPbX_3@ZrH_2P_2O_8$@cellulose composite shows right-handed CPL emissions in solution but left-handed CPL in the solid-state.

The interaction between $FAPbX_3@ZrH_2P_2O_8$ and cellulose occurs through the hydroxyl groups of the cellulose moieties. The formation of right-handed and left-handed helices depends on the H-bonding interaction between the two polymeric cellulose chains. $FAPbX_3@ZrH_2P_2O_8$@cellulose CPL emissions from 430 nm to 650 nm, which is determined by the relative amount of halide anions. As shown in Figure 3d–f, the emission wavelength is tuned from 470 to 640 nm by varying the amount of halide ions, which is consistent with the PL spectrum of all three perovskite composites. The origin of chirality in the $FAPbX_3@ZrH_2P_2O_8$@cellulose composites is extrinsic and arises from the supramolecular helical organization of cellulose fibers rather than from intrinsic chirality of the PNCs or individual glucose units. While glucose monomers are inherently chiral, the linear polymer chains alone do not exhibit macroscopic chirality.[49] Instead, hierarchical self-assembly into helically twisted microfibrils creates a chiral scaffold capable of inducing chiroptical activity.[50] Non-covalent interactions between surface ligands or Pb^{2+} sites of the perovskite NCs and hydroxyl groups of cellulose support efficient chirality transfer without disrupting the structure of either component.[51,52] The appearance of both right- and left-handed CPL signals further confirms that chirality is imposed by the flexible, supramolecular helicity of the cellulose matrix, rather than being intrinsic to the excited states of the perovskite NCs.

3. Conclusion

In summary, this study reports the development of full-color colloidal PNC composites made from pure/mixed halide organic-inorganic hybrid perovskites and inorganic 2D NSs. These were synthesized using phenacyl halide as the sole halide source via a novel surface absorption/ion exchange method. The NCs are grown on 2D-$ZrH_2P_2O_8$ NSs, significantly enhancing their PL QY by 31% for $FAPbBr_{3-x}Cl_x@ZrH_2P_2O_8$, 57.67% for $FAPbBr_3@ZrH_2P_2O_8$, and 26% for $FAPbBr_{3-x}I_x@ZrH_2P_2O_8$ compared to their pure NC counterparts. These materials also demonstrate a high PL intensity even after one year under a humid environment, in contrast to pure NCs, which deteriorated within 30 days. Intriguingly, when the perovskite NCs are embedded within the chiral polymer matrix, they exhibit CD and right-handed and left-handed mirror-image strong CPL across the visible spectrum in solution and solid-state, which is promising for chiro-optoelectronic devices. This chiroptical behavior is attributed to the adaptable chirality of the polymer matrix, which imparts chiroptical properties on the perovskite NCs, which is rarely observed in chiral composite materials. These findings thus offer useful guidelines for the development of efficient chiroptical devices.

4. Experimental Section

Materials: All chemicals were used as received without further purification. Lead (II) oxide (99%) was purchased from TRC, formamidinium acetate (99%) was purchased from Alfa Aesar, and lead (II) bromide (≥ 98%), lead chloride (98%), lead iodide (99%), phenacyl bromide (98%), zirconium (IV) hydrogen phosphate (≥95%), 1-octadecene (tech, 90%), OA (tech, 90%), OAm (tech, 70%), and toluene (99.9%) were purchased from Sigma Aldrich.

Synthesis of $FAPbBr_3$ NCs using Three Precursors: To prepare the FA oleate stock solution, FA oleate (260 mg, 2.5 mmol) was loaded into a 100 ml flask with OA (10 ml). The mixture was maintained in vacuum conditions at 120 °C under stirring for 10 min, then placed in a N_2 atmosphere for 90 min at 120 °C under stirring to obtain a clear yellowish solution. The temperature was reduced to 25 °C and the solution was stored in an N_2 atmosphere.

Synthesis of Green Light-Emitting $FAPbBr_3$ NCs: PbO (0.45 g, 0.2 mmol), phenacyl bromide (0.119 g, 0.6 mmol), OA (1 ml), and 1-octadecene (10 ml) were loaded into a 100 ml flask. The mixture was placed in a vacuum at 120 °C under stirring. After 10 min, N_2 atmosphere was introduced, and the mixture was left for 60 min. The temperature of the reaction mixture was then increased to 220 °C and 0.5 ml of OAm was added to the mixture. The solution turned yellow after annealing for 15 min at 220 °C. The temperature of the reaction mixture was lowered to 50 °C, and 0.5 ml of FA oleate was added to the solution. After 10 s, the reaction system was quenched using an ice-water bath. To collect the final NCs, the solution was centrifuged at 10000 rpm for 10 min and the supernatant was discarded. Alternative synthesis processes using bromide sources such as N-bromosuccinimide and benzoyl bromide have also been reported. However, Patra et al. employed phenacyl bromide to synthesize $FAPbBr_3$ NCs and, in the present study, it was able to optimize the synthesis process and successfully tune the bandgap when synthesizing $FAPbX_3$ NCs using phenacyl bromide.

Synthesis of $FAPbBr_3$ Using Two Precursors: In accordance with a previously reported synthesis method for $FAPbBr_3$, $PbBr_2$ (0.6 mmol) was employed as the source of both lead and bromide. This method substituted the use of PbO and phenacyl bromide as reactants.[29]

Synthesis of $FAPbBr_{3-x}Cl_x$ NCs: $PbCl_2$ (0.166 g, 0.6 mmol) was added to the bromide mixture of phenacyl bromide (0.119 g, 0.6 mmol) as a replacement for PbO in the previously described synthesis method, with the other steps remaining the same.

Synthesis of $FAPbBr_{3-x}I_x$ NCs: PbI_2 (0.277g, 0.6 mmol) was added to the bromide mixture of phenacyl bromide (0.045 g, 0.2 mmol) as a replacement for PbO in the previously described synthesis method, with the other steps remaining the same.

Synthesis of $FAPbX_3@ZrH_2P_2O_8$: Following the typical $FAPbX_3$ synthesis route, 0.2 g $ZrH_2P_2O_8$ (0.7 mmol) was added to the halide mixture and the other steps were kept the same.

Synthesis of $FAPbX_3@ZrH_2P_2O_8$@Cellulose: In this process, 15 mg of cellulose (0.09 mmol) was added to 2 mg of the synthesized $FAPbX_3@ZrH_2P_2O_8$ composite dispersed in toluene. The mixture was then sonicated for 5 min to obtain the $FAPbX_3@ZrH_2P_2O_8$@cellulose composite. For, solid-state chiroptical study, the composite material was deposited onto a glass substrate via drop-casting to fabricate the solid thin-film.

To assess scalability, a batch synthesis was performed to scale up by five times the original quantity. The resulting materials exhibited consistent optical properties, confirming the reproducibility of the synthesis. This robustness stems from the stable precursor chemistry and the modular post-synthetic encapsulation design. Notably, all synthesis steps, such as, halide precursor mixing and integration into $ZrH_2P_2O_8$ NSs were carrried out under N_2 environment, and encapsulation of PNCs within cellulose was conducted under ambient conditions. These features render the protocol compatible with scalable production strategies such as continuous-flow or roll-to-roll processing, provided the appropriate infrastructure is available. The optical properties of the scaled-up samples were included in the Figure S25 (Supporting Information).

Characterization Techniques—Optical Characterization: Spectroflurometer (model: JASCO FP-8500) was used to analyze the PL spectra and PL QY of the samples. The humidity stability of the $FAPbX_3@ZrH_2P_2O_8$ samples was examined by storing them in a moist environment at room temperature, with the PL spectra and PL QY recorded every few hours.

The PL QY is expressed as follows:

$$PLQY = \frac{Number\ of\ photons\ emitted}{Number\ of\ photons\ absorbed} \tag{5}$$

The photo-stability of the $FAPbX_3@ZrH_2P_2O_8$ samples was measured for 35 h. Spectrophotometer (model: JASCO V-770) was used to obtain the UV–vis spectra of the samples, while the CPL spectrometer (model: CPL-300) was used to obtain CPL spectra and the CD spectrometer (model: J-1500-150) was used to obtain CD and ORD spectra.

ORD arises from the differential propagation velocities of left and right CPL. This phenomenon, which was closely correlated with the CD spectrum, frequently exhibits a derivative-like line pattern. This indicates a change in the direction and polarity of the rotation of plane-polarized light at wavelengths corresponding to the peaks observed in the CD spectrum. This method could be used to distinguish the disparate refractive indices produced by substances when exposed to right and left CPL.[56,57] ORD and CD spectra are intrinsically linked because both arise from the same electronic transitions in chiral molecules. Their relationship was formally expressed by the reciprocal Kramers-Kronig relation, which connects the dispersive and absorptive components of optical activity:[57]

$$\varphi(\lambda) = \frac{2}{\pi}\int_0^\infty \theta(\lambda')\,\frac{\lambda'}{\lambda^2 - \lambda'^2}\,d\lambda' \tag{6}$$

$\varphi(\lambda)$ = *CD at wavelength* λ.
$\theta(\lambda')$ = *ORD at wavelength* λ'.
λ = *wavelength at which CD is evaluated.*
λ' = *integration variable representing the wavelength.*

$$\theta(\lambda) = -\frac{2}{\pi\lambda}\int_0^\infty \varphi(\lambda')\,\frac{\lambda'^2}{\lambda^2 - \lambda'^2}\,d\lambda' \tag{7}$$

$\theta(\lambda)$ = *ORD at wavelength* λ'.
$\varphi(\lambda')$ = *CD at wavelength* λ.
λ = *wavelength at which ORD is evaluated.*
λ' = *integration variable representing the wavelength.*

Characterization Techniques—Structural Characterization: TEM images were taken on a JEOL JEM-2100F electron microscope at 200 kV to analyze the morphology and size distribution of the perovskite materials. Samples were prepared on 200-mesh carbon-coated Cu grids using dilute nanowire solutions, which were then allowed to evaporate.

Crystallographic analysis of specimens was conducted using an XRD analyzer with Cu Kα radiation. Powder XRD was performed using Cu Kα radiation (λ = 1.5406 Å). The measurements were taken in a 2θ range of 10° to 50° to identify the crystal structure of the perovskite materials.

The elemental valence states within the samples were identified using XPS (Versaprobe II), while the microstructural characteristics of the samples were examined using field-emission SEM (CLARA LMH). FTIR spectroscopy analysis was conducted using a spectrometer (Nicolet iS50).

Supporting Information

Supporting Information is available from the Wiley Online Library or from the author.

Acknowledgements

This work was supported by the National Research Foundation (NRF) of Korea (BrainLink RS-2023-00236798), and the National Research Foundation of Korea (NRF) grant funded by the Korea government (MSIT) (2021R1A2C1006113).

Conflict of Interest

The authors declare no conflict of interest.

Author Contributions

D.D. designed and conducted all the experiments and performed all the optical measurements. Data analysis was carried out by D.D., Y.P., S.M., A.J., and S.C.Y.P. measured most of the structural characterizations. The original manuscript was written by D.D. and A.J. and edited by Y.P. and S.C. with feedback from all authors. R.T. and K.K. reviewed the manuscript. A.J. conceived the idea. A.J. and S.C. supervised the whole project.

Data Availability Statement

Research data are not shared.

Keywords

circularly polarized luminescence, helical cage, mirror-image, perovskite, tunable, ultrastable

Received: June 11, 2025
Revised: July 15, 2025
Published online:

[1] J. Yao, Z. Wang, Y. Huang, J. Xue, D. Zhang, J. Chen, X. Chen, S. C. Dong, H. Lu, *J. Am. Chem. Soc.* **2024**, *146*, 14157.
[2] A. Pietropaolo, A. Mattoni, G. Pica, M. Fortino, G. Schifino, G. Grancini, *Chem* **2022**, *8*, 1231.
[3] D. Yu, F. Cao, Y. Gao, Y. Xiong, H. Zeng, *Adv. Funct. Mater.* **2018**, *28*, 1800248.
[4] M. P. Hautzinger, X. Pan, S. C. Hayden, J. Y. Ye, Q. Jiang, M. J. Wilson, A. J. Phillips, Y. Dong, E. K. Raulerson, I. A. Leahy, C. S. Jiang, J. L. Blackburn, J. M. Luther, Y. Lu, K. Jungjohann, Z. V. Vardeny, J. J. Berry, K. Alberi, M. C. Beard, *Nature* **2024**, *631*, 307.
[5] B. A. N. Willis, D. Schnable, N. D. Schley, G. Ung, *J. Am. Chem. Soc.* **2022**, *144*, 22421.
[6] Y. Tanaka, T. Murayama, A. Muranaka, E. Imai, M. Uchiyama, *Chem. - A Eur. J.* **2020**, *26*, 1768.
[7] Y. Zhong, Z. Wu, Y. Zhang, B. Dong, X. Bai, *InfoMat* **2023**, *5*, 12392.

[8] A. Dutta, R. K. Behera, P. Pal, S. Baitalik, N. Pradhan, *Angew. Chem., Int. Ed.* **2019**, *58*, 5552.
[9] N. Mondal, A. De, A. Samanta, *ACS Energy Lett.* **2019**, *4*, 32.
[10] H. Zhu, M. Cheng, J. Li, S. Yang, X. Tao, Y. Yu, Y. Jiang, *Chem. Eng. J.* **2021**, *428*, 130974.
[11] Y. Ru, B. Zhang, X. Yong, L. Sui, J. Yu, H. Song, S. Lu, *Adv. Mater.* **2023**, *35*, 2207265.
[12] S. Lin, Y. Tang, W. Kang, H. K. Bisoyi, J. Guo, Q. Li, *Nat. Commun.* **2023**, *14*, 3005.
[13] S. Li, X. Xu, C. A. Kocoj, C. Zhou, Y. Li, D. Chen, J. A. Bennett, S. Liu, L. Quan, S. Sarker, M. Liu, D. Y. Qiu, P. Guo, *Nat. Commun.* **2024**, *15*, 2573.
[14] Y. Cho, H. R. Jung, W. Jo, *Nanoscale* **2022**, *14*, 9248.
[15] E. I. Jung, H. J. Lee, J. Kim, Q. T. Siddiqui, M. Kim, Z. Lin, C. Park, D. H. Kim, *Mater. Sci. Eng. R Rep.* **2024**, *160*, 100817.
[16] J. Hu, S. Zhu, M. Gu, Y. Zhang, *ACS Photonics* **2024**, *11*, 2007.
[17] W. Yue, H. Yang, H. Cai, Y. Xiong, T. Zhou, Y. Liu, J. Zhao, F. Huang, Y. B. Cheng, J. Zhong, *Adv. Mater.* **2023**, *35*, 2301548.
[18] R. A. John, N. Shah, S. K. Vishwanath, S. E. Ng, B. Febriansyah, M. Jagadeeswararao, C. H. Chang, A. Basu, N. Mathews, *Nat. Commun.* **2021**, *12*, 3681.
[19] Y. H. Kim, Y. Zhai, E. A. Gaulding, S. N. Habisreutinger, T. Moot, B. A. Rosales, H. Lu, A. Hazarika, R. Brunecky, L. M. Wheeler, J. J. Berry, M. C. Beard, J. M. Luther, *ACS Nano* **2020**, *14*, 8816.
[20] L. Tao, H. Zhan, Y. Cheng, C. Qin, L. Wang, *J. Phys. Chem. Lett.* **2023**, *14*, 2317.
[21] B. Zhao, X. Gao, K. Pan, J. Deng, *ACS Nano* **2021**, *15*, 7463.
[22] S. Zhao, Y. Yu, B. Zhang, P. Feng, C. Dang, M. Li, L. Zhao, L. Gao, *Colloids Surf., A* **2022**, *645*, 128921.
[23] C. Yang, W. Niu, R. Chen, T. Pang, J. Lin, Y. Zheng, R. Zhang, Z. Wang, P. Huang, F. Huang, D. Chen, *Adv. Mater. Technol.* **2022**, *7*, 2200100.
[24] C. Romero-Pérez, N. F. Delgado, M. Herrera-Collado, M. E. Calvo, H. Míguez, *Chem. Mater.* **2023**, *35*, 5541.
[25] B. Huo, J. Yang, Y. Bian, D. Wu, J. Feng, J. Zhou, Q. Huang, F. Dong, X. Tang, *Chem. Eng. J.* **2021**, *406*, 126740.
[26] R. Thakkar, H. Patel, U. Chudasama, *Bull. Mater. Sci.* **2007**, *30*, 205.
[27] I. Levchuk, A. Osvet, X. Tang, M. Brandl, J. D. Perea, F. Hoegl, G. J. Matt, R. Hock, M. Batentschuk, C. J. Brabec, *Nano Lett.* **2017**, *17*, 2765.
[28] Y. L. Tong, Y. W. Zhang, K. Ma, R. Cheng, F. Wang, S. Chen, *ACS Appl. Mater. Interfaces* **2018**, *10*, 31603.
[29] A. Patra, S. Bera, D. Nasipuri, S. K. Dutta, N. Pradhan, *ACS Energy Lett.* **2021**, *6*, 2682.
[30] Y. R. Park, S. Eom, H. H. Kim, W. K. Choi, Y. Kang, *Sci. Rep.* **2020**, *10*, 14758.
[31] A. Siddik, P. K. Haldar, U. Das, A. Roy, P. K. Sarkar, *Mater. Chem. Phys.* **2023**, *297*, 127292.
[32] F. Zhang, H. Zhong, C. Chen, X. G. Wu, X. Hu, H. Huang, J. Han, B. Zou, Y. Dong, *ACS Nano* **2015**, *9*, 4533.
[33] S. Gonzalez-Carrero, R. E. Galian, J. Pérez-Prieto, *J. Mater. Chem. A* **2015**, *3*, 9187.
[34] J. D. McGettrick, K. Hooper, A. Pockett, J. Baker, J. Troughton, M. Carnie, T. Watson, *Mater. Lett.* **2019**, *251*, 98.
[35] D. Briggs, *Handbook of Adhesion*, 2nd ed., John Wiley and Sons, Hoboken, NJ **2005**, p. 621.
[36] A. Maqsood, Y. Li, J. Meng, D. Song, B. Qiao, S. Zhao, Z. Xu, *Nanoscale Res. Lett.* **2020**, *15*, 89.
[37] S. R. Teeparthi, E. W. Awin, R. Kumar, *Sci. Rep.* **2018**, *8*, 5541.
[38] D. R. Do Carmo, T. F. S. da Silveira, *J. Inorg. Organomet. Polym. Mater.* **2019**, *29*, 1205.
[39] A. Clearfield, J. A. Stynes, *J. Inorg. Nucl. Chem.* **1964**, *26*, 117.
[40] A. Clearfield, J. M. Troup, *J. Phys. Chem.* **1973**, *77*, 243.
[41] V. K. Ravi, G. B. Markad, A. Nag, *ACS Energy Lett.* **2016**, *1*, 665.
[42] E. J. Juarez-Perez, L. K. Ono, Y. Qi, *J. Mater. Chem. A.* **2019**, *7*, 16912.
[43] A. Mayer, N. Pourdavoud, Z. Doukkali, K. Brinkmann, J. Rond, J. Staabs, A. C. Swertz, F. van gen Hassend, P. Görrn, T. Riedl, H. C. Scheer, *Appl. Phys. A Mater. Sci. Process.* **2021**, *127*, 237.
[44] S. Choi, S. Y. Lee, D. Y. Kim, H. K. Park, M. J. Ko, K. H. Cho, J. Choi, *J. Ind. Eng. Chem.* **2020**, *85*, 226.
[45] A. Jana, K. S. Kim, *ACS Energy Lett.* **2018**, *3*, 2120.
[46] S. Premkumar, K. Kundu, S. Umapathy, *Nanoscale* **2019**, *11*, 10292.
[47] W. Mu, Q. Yu, J. Gu, X. Li, Y. Yang, H. Wei, S. Peng, *Sep. Purif. Technol.* **2020**, *240*, 116658.
[48] A. O. Rajeh, L. Szirtes, *J. Radioanal. Nucl. Chem.* **1999**, *241*, 83.
[49] G. Fittolani, D. Vargová, P. H. Seeberger, Y. Ogawa, M. Delbianco, *J. Am. Chem. Soc.* **2022**, *144*, 12469.
[50] M. Khandelwal, A. Windle, *Carbohydr. Polym.* **2014**, *106*, 128.
[51] J. Zhang, Z. Ding, X. Liu, Z. He, Y. Chen, S. Cai, J. Wang, G. Li, Y. Liu, *ACS Appl. Mater. Interfaces* **2024**, *16*, 36811.
[52] M. Wohlert, T. Benselfelt, L. Wågberg, I. Furó, L. A. Berglund, J. Wohlert, *Cellulose* **2022**, *29*, 1.
[53] R. B. Cundall, T. F. Palmer, *Annu. Reports Prog. Chem. Sect. A Phys. Inorg. Chem.* **1973**, *70*, 31.
[54] M. Kim, J. Kim, J. Bang, Y. J. Jang, J. H. Park, D. H. Kim, *J. Mater. Chem. A.* **2023**, *11*, 12876.
[55] S. M. Kelly, T. J. Jess, N. C. Price, *Biochim. Biophys. Acta - Proteins Proteomics* **2005**, *1751*, 119.
[56] C. A. Emeis, L. J. Oosterhoff, *Chem. Phys. Lett.* **1967**, *1*, 129.
[57] H. Eyring, H. C. Liu, D. Caldwell, *Chem. Rev.* **1968**, *68*, 525.
[58] A. Taniguchi, D. Kaji, N. Hara, R. Murata, S. Akiyama, T. Harada, A. Sudo, H. Nishikawa, Y. Imai, *RSC Adv.* **2019**, *9*, 1976.
[59] K. Nakabayashi, T. Amako, N. Tajima, M. Fujiki, Y. Imai, *Chem. Commun.* **2014**, *50*, 13228.
[60] Z. Li, W. Li, D. Li, W. Tang, H. Liang, H. Song, C. Chen, L. Gao, J. Tang, *Front. Optoelectron.* **2024**, *17*, 1.